Effects of using a logarithmic formulation for the length-scale equation in RANS turbulence models

K. Chandrasekar Jeyanthi*, T. Knopp*, A. Probst*, R.I. Sánchez-Ortiz*, U S Vevek**, C. Grabe*
Corresponding author: keerthana.chandrasekarjeyanthi@dlr.de
* $C^2A^2S^2E^2$, Institute for Aerodynamics and Flow Control, DLR, Göttingen, Germany.
**Airbus Operations Ltd, Bristol, BS34 7PA, United Kingdom

Abstract: The logarithmic formulation (log form) of the length-scale equation in two-equation turbulence models is a well-known approach to guarantee the positivity of the length-scale variable specifically in the transient phase of simulations. Although the log form is known to improve robustness, it has been reported that the converged solution can differ from the non-logarithmic formulation (non-log form) depending on the mesh refinement. These differences in the solution become important when judging and comparing results from both forms on practical meshes with limited resolution, as typically required by industry. For that reason, a recently-started migration from one flow solver with the non-log form of the SST model to a new solver featuring its log-form has led to a joint verification-and-validation campaign by academic and industrial partners. This campaign included the following studies on a) the implementation of the turbulence models, b) assessment of the mesh convergence behavior, c) the impact of the discretization settings on both robustness and accuracy. In this paper, we aim to describe the results of our investigations and show that the log form improved the robustness and y^+ sensitivity but also showed some sensitivities to discretization settings and the implementation details.

Keywords: Two-equation turbulence models, length-scale equation, robustness, validation, implicit solvers

1. Introduction

Recent decades have seen substantial advancements in several areas such as computing infrastructure, applied numerical mathematics, software design, physical modelling alongside the industrial needs to re-engineer workflows for optimizing operational cost, product development cycles and other business competitiveness drivers. Such advancements naturally compel the up-gradation of the industrial engineering tools from legacy frameworks to advanced platforms. Computational fluid dynamics (CFD) has been one of the critical tools for evaluating and optimizing aircraft design. Transitioning from legacy to the next generation CFD solvers is constrained by rigorous regulatory certification frameworks where the advanced numerical formulations introduce basic discrepancies and validation complexities. Industrial CFD solvers require Reynolds-Averaged Navier Stokes (RANS) based turbulence models to meet their the day to day simulation needs. Hence, evaluation of these models in the new solver framework is one of the first steps during the transition process. Aerospace industries have stringent accuracy requirements where advanced turbulence models are necessary for better prediction of the physics. One of the widely used turbulence models is the Menter's Shear Stress Transport model (SST)[1]. While the underlying physics of the SST model remain constant, the mathematical and numerical implementation often differ significantly among different solvers causing discrepancies in aerodynamic coefficients and flow topologies. Therefore, an evaluation of the model implemented into a new solver is required through the verification and validation processes across the relevant flow regimes using industrial grade meshes. While performing these activites one of the major elements that differed from our previous legacy solver (DLR-TAU [2]) to the next generation solver (CODA [3]) was the usage of the logarithmic (log) form of the length scale equation in the SST turbulence model. The motivation behind its usage arises from several reported benefits such as improved stability, iterative convergence, error convergence and acceptable differences in the solution compared to the standard SST model [4] [5] [6]. The previous studies have also mentioned the need for verification and validation of the log formulation [7] to ensure that the discrepancies are well understood. However, there is a lack of such studies in the literature.

This paper addresses these differences found between the two formulations of the length scale equation and the dependency of these formulations on the implementation details, the solver settings and mesh refinement. One of the ways to understand the discretization errors arising from the two formulations is to perform mesh convergence studies for various cases in different flow regimes. A mesh convergence study done by Braun [5] on the NACA0012 airfoil for the Reynolds stress models in the DLR-TAU solver shows that the $\ln(\omega)$ variant generates large deviations in the lift and drag coefficients on the coarser mesh that vanish under grid refinement. As industrial grade meshes fall under the coarser mesh levels used in these mesh convergence studies, we also use these mesh convergence studies to explain the differences which the users may encounter when transitioning from a legacy code to next generation solvers.

The content of the paper is organised as follows:

Section 2 Describes the SST model and the length-scale equation formulation

Section 3 Formulates the details involved in implementation of the model such as the usage of realizability limiters, clipping approximations, neglect of terms for compressible flows and sustaining turbulence.

Section 4 Outlines the details of the legacy and the new solver such as discretization settings (convection schemes, gradient computation, gradient limiters) and time integration settings.

Section 5 Provides details on the cases and meshes where the differences were first observed, leading to our further studies involving verification and mesh refinement studies

Section 6 Depicts the first observed difference in the far-field decay behaviour when using industrial meshes, the results from the mesh convergence studies performed on different flow regimes, effect of mesh refinement in the near wall and boundary layer and the effects on shock position arising from discretization settings and trailing edge mesh refinement.

2. Two-equation Menter's shear stress transport (SST) model

Menter introduced the SST model in 1994 to overcome the limitations of the standard two-equation models by combining the strengths of k–ω and k–ϵ formulations using blending functions. The model is based on the Wilcox k–ω [8] turbulence model in the near-wall region which avoids problematic damping functions while it provides good capabilities to predict adverse pressure gradient flows, the ability to use simple Dirichlet boundary conditions and beneficial numerical stability. It transitions smoothly to the k–ϵ formulation in the outer boundary layer to the free-stream, thereby eliminating the sensitivity of the k–ω model to free-stream values of ω_f specified for ω outside the boundary layer. From this Menter baseline model (BSL) [1], Menter modified the eddy viscosity to account for the transport of the principal shear stresses needed in adverse pressure gradient flows leading to the shear stress transport (SST) model. The SST model was then widely adopted as a standard eddy viscosity model (EVM) due to its robustness, predictive capabilities and extensions like scale adaptive simulations and laminar–turbulent transition modeling [9]. Although the SST model has improved capabilities compared to the other EVMs, it falls short to correctly predict strong adverse pressure gradients with secondary flows, large separation regions, vortex dominated flows where one has to move from the class of EVMs to more advanced models like Differential Reynolds stress models (RSM). However, RSMs are usually not as robust as EVMs and they come with additional computing cost for solving more equations for all Reynolds stresses.

2.1 The ω-based version

The equations for the SST model originally published by Menter in 1994 [1] as pubished on the NASA Turbulence Modelling Resource (TMR) [1] for the turbulent kinetic energy k and for the turbulent dissipation rate ω are given by:

$$\frac{\partial(\overline{\rho}k)}{\partial t} + \frac{\partial}{\partial x_j}\left(\overline{\rho}U_j k\right) = P_k - \beta^*\overline{\rho}k\omega + \frac{\partial}{\partial x_j}\left((\mu + \sigma_k\mu_t)\frac{\partial k}{\partial x_j}\right), \tag{1}$$

$$\frac{\partial(\overline{\rho}\omega)}{\partial t} + \frac{\partial}{\partial x_j}\left(\overline{\rho}U_j\omega\right) = \frac{\gamma}{\nu_t}P_k - \beta\overline{\rho}\omega^2 + \frac{\partial}{\partial x_j}\left((\mu + \sigma_\omega\mu_t)\frac{\partial \omega}{\partial x_j}\right) + 2(1-F_1)\frac{\overline{\rho}\sigma_{\omega 2}}{\omega}\frac{\partial k}{\partial x_j}\frac{\partial \omega}{\partial x_j} \tag{2}$$

with the production term P_k given by

$$P_k = \tau_{ij}^{\text{turb}}\frac{\partial U_i}{\partial x_j} \tag{3}$$

$$\tau_{ij} = \mu_t\left(2S_{ij} - \frac{2}{3}\frac{\partial U_k}{\partial x_k}\right) - \frac{2}{3}\rho k\delta_{ij} \tag{4}$$

where $\overline{\rho}$ is the density, k is the turbulent kinetic energy, ω is the turbulent frequency, U_i is the flow velocity, μ_t is the eddy viscosity, S is the invariant measure of strain rate defined below in eq. (10). The latter relation (4) is the Boussinesq hypothesis. F_1 and F_2 are blending functions which are 0 away from the surface (k–ϵ model active) and 1 inside the boundary layer (k–ω model active). Each of the model constants is blended using $\phi = F_1\phi_1 + (1-F_1)\phi_2$. The blending functions and the cross diffusion term are given by

$$F_1 = \tanh\left(\text{arg}_1^4\right), \quad F_2 = \tanh\left(\text{arg}_2^2\right), \tag{5}$$

$$\text{arg}_1 = \min\left[\max\left(\frac{\sqrt{k}}{\beta^*\omega d}, \frac{500\nu}{d^2\omega}\right), \frac{4\overline{\rho}\sigma_{\omega 2}k}{CD_{k\omega}d^2}\right], \quad \text{arg}_2 = \max\left(\frac{2\sqrt{k}}{\beta^*\omega d}, \frac{500\nu}{d^2\omega}\right) \tag{6}$$

$$CD_{k\omega} = \max\left(2\overline{\rho}\sigma_{\omega 2}\frac{1}{\omega}\frac{\partial k}{\partial x_j}\frac{\partial \omega}{\partial x_j}, 10^{-20}\right) \tag{7}$$

where d is the distance from the wall. It was also recommended to used the production limiter [10] to prevent the build up of turbulence in the stagnation region given as:

$$\tilde{P_k} = min(P_k, 20\cdot\beta^\star\rho k\omega) \tag{8}$$

Differences in terms	SST1994	SST2003
Eddy viscosity (μ_t)	$\frac{\overline{\rho}a_1 k}{\max(a_1\omega, \Omega F_2)}$	$\frac{\overline{\rho}a_1 k}{\max(a_1\omega, SF_2)}$
Cross diffusion ($CD_{k\omega}$)	$\max\left(2\overline{\rho}\sigma_{\omega 2}\frac{1}{\omega}\frac{\partial k}{\partial x_j}\frac{\partial \omega}{\partial x_j}, 10^{-20}\right)$	$\max\left(2\overline{\rho}\sigma_{\omega 2}\frac{1}{\omega}\frac{\partial k}{\partial x_j}\frac{\partial \omega}{\partial x_j}, 10^{-10}\right)$
Production limiter ($\tilde{P_k}$)	$min(P_k, 20\cdot\beta^\star\rho k\omega)$	$min(P_k, 10\cdot\beta^\star\rho k\omega)$

Table 1: Differences in the various terms of the two SST versions - 1994 and 2003

[1] https://tmbwg.github.io/turbmodels/sst.html

After the publication of the original model, Menter modified the SST model through robustness optimization leading to the 2003 version which will be referred in this paper as SST2003. Hence the above stated model will be referred to as the SST1994 (1994 version) and the differences between these versions are listed in the Table 1

where,

$$\Omega_{ij} = \frac{1}{2}\left(\frac{\partial U_i}{\partial x_j} - \frac{\partial U_j}{\partial x_i}\right), \quad \Omega = \left(2\Omega_{ij}\Omega_{ij}\right)^{1/2} . \tag{9}$$

$$S_{ij} = \frac{1}{2}\left(\frac{\partial U_i}{\partial x_j} + \frac{\partial U_j}{\partial x_i}\right), \quad S = \left(2S_{ij}S_{ij}\right)^{1/2} . \tag{10}$$

The constants (ϕ_1, ϕ_2) used for the model are $\beta_1 = 0.075, \sigma_{k1} = 0.85, \sigma_{\omega 1} = 0.5, \beta_2 = 0.0828, \sigma_{k2} = 1.0, \sigma_{\omega 2} = 0.856$. The other constants used are $\beta^\star = 0.09, \kappa = 0.41, a_1 = 0.31$.

2.2 Logarithmic (log) formulation of the length-scale equation

The log formulation of the length-scale equation ($\ln(\omega)$) had been previously implemented in the DLR-TAU legacy solver for the Reynolds stress models [5] and had been reported to improve robustness across various flow regimes and varying complexity through verification studies. Further more, the new solver CODA [3] provides a combined framework for both finite volume (FV) and discrete Galerkin (DG) methods, thereby making the log formulation essential in CODA. The transport equation for $\hat{\omega} \equiv \ln(\omega)$ (or: $\omega = e^{\hat{\omega}}$) follows from

$$\frac{D\hat{\omega}}{Dt} = \frac{D\hat{\omega}}{D\omega}\frac{D\omega}{Dt} = \frac{1}{\omega}\frac{D\omega}{Dt} = \frac{1}{e^{\hat{\omega}}}\frac{D\omega}{Dt} \tag{11}$$

Then multiplication of the ω-equation with $1/e^{\hat{\omega}}$ and substituting ω for $e^{\hat{\omega}}$ yields

$$\begin{aligned} \frac{\partial(\overline{\rho}\hat{\omega})}{\partial t} + \frac{\partial}{\partial x_j}\left(\overline{\rho}U_j\hat{\omega}\right) = {} & \frac{1}{e^{\hat{\omega}}}\frac{\gamma}{\nu_t}P_k - \beta\overline{\rho}e^{\hat{\omega}} + \frac{\partial}{\partial x_j}\left(\left(\mu + \sigma_\omega\mu_t\right)\frac{\partial\hat{\omega}}{\partial x_j}\right) \\ & + \left(\mu + \sigma_\omega\mu_t\right)\frac{\partial\hat{\omega}}{\partial x_j}\frac{\partial\hat{\omega}}{\partial x_j} + \frac{1}{e^{\hat{\omega}}}2(1 - F_1)\overline{\rho}\sigma_{\omega 2}\frac{\partial k}{\partial x_j}\frac{\partial\hat{\omega}}{\partial x_j} \end{aligned} \tag{12}$$

For the computation of the turbulent viscosity, again a form of the SST limiter is applied, i.e., for the SST-2003 model

$$\mu_t = \frac{\overline{\rho}a_1 k}{\max\left(a_1 e^{\hat{\omega}}, SF_2\right)} \tag{13}$$

Note that in the $\hat{\omega}$-equation, an additional term arises compared to the ω-equation, emerging from the transformation of the turbulent diffusion term given as:

$$\frac{\partial}{\partial x_j}\left(\left(\mu + \sigma_\omega\mu_t\right)\omega\frac{\partial\hat{\omega}}{\partial x_j}\right) = \omega\left(\mu + \sigma_\omega\mu_t\right)\frac{\partial\hat{\omega}}{\partial x_j}\frac{\partial\hat{\omega}}{\partial x_j} + \omega\frac{\partial}{\partial x_j}\left(\left(\mu + \sigma_\omega\mu_t\right)\frac{\partial\hat{\omega}}{\partial x_j}\right) \tag{14}$$

2.3 Boundary conditions for turbulence equations

Finally, we considered the boundary conditions for k and ω or $ln(\omega)$. For the k equation, the standard condition is $k|_w = 0$ at the wall. Another possible boundary condition is $\partial k/\partial n = 0$ with n denoting the normal direction. The latter condition follows from the definition of k and from the no-slip condition for the velocity fluctuations, and so the theoretical k has a quadratic zero at the wall (see [11] p. 124). Concerning ω, the boundary condition proposed by Menter is to impose a value of $\omega|_w = C_{wf}6\nu/(\beta y_1^2)$ at the wall which uses the analytical flat plate turbulent boundary at zero-pressure gradient solution of ω in the viscous sublayer (see [11]). The method uses the value computed at the wall distance of the first grid node and uses for extrapolation to the wall a so-called wall factor for ω of $C_{wf} = 10$. A study of the extrapolation factor and possible adjustment depending on the underlying numerical scheme can be found in [12]. An alternative boundary condition [13] is a so-called hybrid wall-function boundary condition, which uses a blending of the viscous-sublayer solution and of the log-layer solution of ω in a zero-pressure gradient turbulent boundary layer. This boundary condition gives a meaningful ω-value even if the first node above the wall is located above the viscous sublayer. For a mesh with $y^+ < 1$, both boundary conditions for ω cannot be distinguished.

3. Implementation aspects of the SST model

3.1 Clipping for k and ω

Ensuring positivity of turbulence variables has always been important in the implementation of the turbulence models. This is usually achieved by the classical clipping approximation technique [14] where the variables are limited to some small fraction of their respective reference values. Even though the log form guarantees the positivity of the length scale equation, it is possible that $ln(\omega)$ when transformed to ω to calculate some terms like eddy viscosity in the equation, ω can take very small values which affect robustness in industrial solvers. Hence, we also additionally clip the log form in $ln(\omega)$ when needed. The clipping factors are set to 10^{-8} for k and and 10^{-5} for ω in the non-log form. While using the log form, the clipping is always done after transforming it to ω. When cases from suffer convergence issues, $ln(\omega)$ is also clipped with a factor of 10^{-5}. Otherwise, the clipping factor is set to machine epsilon for $ln(\omega)$.

3.2 Realizability conditions

Although positivity preservation ensures the positivity of turbulence variables, when considering the whole Reynolds stress tensor $\tau_{ij}^{turb} = \overline{\rho u_i'' u_j''}$, it may not guarantee the physicality of the tensor. Realizability violations of the Reynolds-stress tensor can occur in the solution of the two equation models. Durbin [15] explain this as the reason towards the stagnation point anomaly observed in two equation models and formulated a time-scale limiter for the $k - \epsilon$ model as one of the potential ways to solve it. Although Menter SST uses a production limiter for the stagnation point anomaly issue, the realizability limiter imposes a stricter limitation and has helped in the robustness of the legacy solver for certain difficult cases. The legacy solver applied the limiter (see Appendix A) to ω with the non-log form directly and clipped ω to a higher value than the clipping described in the previous Section 3.1. During the verification experiments, some deviations between the log and the non-log formulations occurred skin friction C_f profile at the leading edge. Initially, we did not concentrate much as it occurred in the pseudo-laminar region, however when the realizability limiter was turned off, these differences disappeared. This lead to a closer observation and the use of the realizability constraints by clipping directly at $ln(\omega)$ were found to cause not just the leading edge C_f deviation but also some weird blobs in the blending function F_2 of the SST model. These weird blobs were also found when using the non-log form but was were visible in the log form. The realizability constraints were however important for robustness, hence we took a closer look at the derivation of the realizability constraints from Durbin's work [15] which is described in the Appendix B. The realizability constraints were then only in the turbulent eddy viscosity in CODA given by,

$$\mu_t = \frac{\overline{\rho} a_1 k}{\max\left(a_1 \max\left(\omega,\ \sqrt{6}|\widetilde{S}|\right),\ \Omega F_2\right)}. \tag{15}$$

It must be emphasised that the lower bound is only used in μ_t whereas the positivity-enforced clipped values are used in μ_t for the source terms (i.e., the dissipation of k and ω).

3.3 Limitation of turbulent source terms

The unlimited production term P_k in Eq. 3 can be expanded and re-written as follows.

$$P_k = 2\mu_t |\widetilde{S}|^2 - \frac{2}{3}\rho k \frac{\partial U_k}{\partial x_k} \tag{16}$$

The second term in the above result could become negative when the dilatation is positive and for a small enough μ_t, it may even cause P_k to become negative. To avoid such a situation, the second term was omitted from the calculation of the production term.

One of the differences between the SST1994 and SST2003 model is that the SST2003 model uses limited production $\tilde{P}_k$ (as in Table 1) for both k and ω equations. Use of the limited production in the ω equation leads to a more gradual increase in ω from free-stream when approaching the stagnation point. This, in turn, leads to the blending factor F_1 increasing to 1 much further away from the wall for the SST2003 model compared to its predecessor. To suppress such "ghost" shear layers with $F_1 \approx 1$, the unlimited production term was used in the ω equation for both models. Use of the realizability (Durbin) limiter along with disabling the production limiter in the length-scale equation were later found to be important for improving the robustness of the log form in the new solver. The use of unlimited production for the ω equations has also been mentioned in the work of Evans et al [16] in the commercial STAR-CCM+ solver where they replace the production limitation in the k equation as well with the Durbin limiter. Such studies in the k equation are aimed as future work in the new solver.

3.4 Sustaining turbulence

The far-field behaviour of the turbulence equations can be analysed by assuming a steady flow with a stream-wise velocity of $U_\infty > 0$ along the x-axis. Further assuming that the diffusion and cross-diffusion terms are negligible, Eqs. (1) and (2) reduce to the following coupled ordinary differential equations.

$$\frac{dk}{dx} = -\frac{\beta^* k\omega}{U_\infty}, \qquad \frac{d\omega}{dx} = -\frac{\beta_2 \omega^2}{U_\infty} \tag{17}$$

Note that we have substituted $\beta = \beta_2$ in the ω equation as we are far away from the walls and $F_1 = 0$.

These equations can be solved analytically to obtain the variations of k, ω and ν_t in terms of the farfield values k_∞ and ω_∞ along the x-axis whereby $x = 0$ denotes the farfield boundary:

$$k(x) = k_\infty \left(1 + \frac{\beta_2 \omega_\infty}{U_\infty} x\right)^{-\frac{\beta^*}{\beta_2}}, \qquad \omega(x) = \omega_\infty \left(1 + \frac{\beta_2 \omega_\infty}{U_\infty} x\right)^{-1} \tag{18}$$

Both quantities decay from their far-field values as x increases. Since $\beta^*/\beta_2 > 1$, k decays faster than ω and since the turbulent viscosity scales as their ratio, it decays as well. The far-field values are prescribed using a turbulence intensity of $I_t = 10^{-3}$ (with I_t defined by $I_t^2 = (2/3)k/U_\infty^2$) and a turbulent viscosity ratio of $\mu_t/\mu = 0.1$ based on the recommendations in e.g. [17]. These values ensure that the decayed turbulence levels are sufficiently low when the flow comes into contact with the body but the exact levels depend on the far-field distance. The decay near the far-field boundary can be quite drastic and typical far-field grid resolutions are not adequate to capture this accurately. Since μ_t depends on the ratio of k to ω, even slight changes in their decay rates can significantly alter the behaviour of μ_t. During early investigations, it was observed that the log form was particularly susceptible to this problem, sometimes even predicting an initial spike in μ_t before the decay. Moreover, spurious striations of μ_t were observed to propagate far into the computational domain which are shown in the section 6.1

The sustaining turbulence (SUST) variant of the SST model, described by Spalart and Rumsey [17], was considered as a solution to overcome this problem. The SUST variant involves adding the following source terms to Eqs. (1) and (2), respectively, to counteract the destruction terms and, consequently, *sustain* the far-field turbulence levels along the free stream.

$$P_k^{\text{SUST}} = \beta^* k_\infty \omega_\infty, \qquad P_\omega^{\text{SUST}} = \beta \omega_\infty^2 \tag{19}$$

The far-field values for the SUST variant were prescribed using $I_t = \sqrt{2/3} \times 10^{-3}$ and $\mu_t/\mu = 2 \times 10^{-7} Re$ based on the recommendations. [17]

In addition to avoiding the far-field decay, the SUST variant also improved the robustness of the simulations, sometimes quite dramatically. However, the SUST terms rapidly destroyed the turbulence in the wake when using the recommended free-stream conditions. While the recommended value for k_∞ is smaller than k in the wake,the recommended value for ω_∞ is greater than ω in the wake. The higher value of ω_∞ increases the production of $\overline{\rho}\omega$ through the P_ω^{SUST} term. As $\overline{\rho}\omega$ increases, it causes the destruction term of $\overline{\rho}k$ to increase. This production of $\overline{\rho}\omega$ and the destruction of $\overline{\rho}k$ continues until they return to their respective free-stream levels upon which the destruction and SUST terms balance each other. Using much smaller far-field values preserved the turbulence in the wake but the robustness suffered significantly.

3.4.1 Wake-preserving sustaining turbulence

In order to capture the correct behaviour in the wake while maintaining the recommended free-stream turbulence levels for the sake of solver stability, a modified free-stream turbulence dissipation rate

$$\omega_\infty^{\mathrm{WP}} = \omega_\infty \exp\left[-16\left(\frac{\max(k, k_\infty) - k_\infty}{k_\infty}\right)^2\right] \tag{20}$$

is used instead of ω_∞ in Eq. (19). The rationale for the modification is that the SUST terms are only required in the free-stream where $k = k_\infty$ and they can be deactivated as soon as k exceeds k_∞ to avoid interfering in the other regions. Since a higher value of ω_∞ is the main driver in the destruction of the turbulence in the wake, the Gaussian cutoff function in Eq. (20) acts on ω_∞ leading to a faster suppression of P_ω^{SUST}. Note that the SUST terms are not suppressed when $k < k_\infty$ such as near the wall. Alternatives to Eq. (20) involving the blending factor F_1 to suppress the SUST terms near the wall were also explored but these had little impact on the final results as the SUST terms are dominated by the destruction terms near the wall. Therefore, the above form was retained for simplicity. The constant 16 was chosen through numerical experiments. The modified formulation is referred to as wake-preserving (WP) sustaining turbulence.

4. CFD Software description

4.1 CFD Software CODA

The initial version of the next-generation CFD solver known as Flucs (Flexible Unstructured CFD Software) was initiated at DLR to advance industrial simulation methods and enable virtual flight envelope exploration, focusing on higher-order methods, implicit schemes, HPC parallelization, and modern software principles [18]. As adoption grew among industrial and European partners, the CFD Software by ONERA, DLR and Airbus (CODA) was developed based on Flucs. [3]

4.1.1 Spatial discretization:

CODA uses a cell centred finite volume (FV) approach supporting unstructured 3D meshes. Although the solver provides a framework combining FV and DG discretization methods, we focus only on FV for this paper. The mean flow convective fluxes are calculated using the Roe upwinding scheme where a minimal dissipation (entropy-fix) can be enforced when needed. For the turbulence equations, Roe upwinding scheme for transport equations were initially used which led to some stability issues, so we switched to the usage of a simple upwinding scheme for turbulence equations. For 2^{nd} order flux calculations, linear reconstruction using extended Green–Gauss gradients [19] are used. The diffusion terms are calculated using a central scheme by averaging the fluxes from the right and left elements, where the face gradients are computed as average of adjacent element gradients and subsequently augmented with a finite difference formula. Consistency of the calculations can be improved by using linear reconstruction and non-linear limiters (described below) are sometimes used for stability. During our validation campaign, we found one of the reasons we suffered from robustness issues for SST simulations with second order accuracy was arose from the gradient limiters which was in use. Inspired from our legacy solver TAU, we modified our gradient limiters such that we can impose different limitations on the mean flow and turbulent equations. It was found as one of the key elements to improve our robustness but additionally it had an effect on the accuracy of the log form for some cases (described in section 6.2.3).

Gradient limitation: In the classical formulation of linear reconstructions, the gradient limiters contain a small regularization factor ε, which is typically scaled with the local mesh size. In the current work, this is replaced by a solution-dependent factor so that the limiter becomes attenuated in smooth regions while keeping its original behavior in regions of strong gradients. This factor is further scaled by a parameter, K_{sd}, to control the strength of the attenuation. High attenuation of the gradient limiters, given by values of 10^{-2} or 10^{-3}, was necessary to provide second order accuracy in space. However, too strong attenuation levels caused the gradient limiters to fail to prevent the creation of new extrema for the turbulent variables, such as non-physical undershoots and negative values of k, negatively affecting the robustness of the numerical scheme. To avoid excessive attenuation while maintaining a non-zero regularization factor for a well-defined limiter formulation, an attenuation factor of 10^{-14} is used for the turbulent variables. Having these different attenuation levels for mean flow and turbulent variables proved to be a compromise in the gradient limitation, keeping second order accuracy in space and a robust behavior.

4.1.2 Time integration:

CODA implements a fully implicit scheme (implicit Euler method) for pseudo time integration with local time stepping for solving steady state problems. CODA also offers automatic differentiation (AD) for generating the Jacobian through residual evaluation. However, a matrix based Jacobian offered more robustness during the pseudo-transient phase and also led to performance improvements for the two equation turbulence models. Initially a matrix-free AD was a necessity beyond the pseudo-transient phase to obtain residual convergence. Later, the Runge-Kutta implicit method [20] was found to remove the need of matrix-free AD for most cases and further improve robustness. Still, some cases performed better with the implicit Euler method and matrix-free AD was strictly needed to obtain convergence. Hence, for the simulations results discussed in section 6, we have used the Runge-Kutta implicit scheme for most of the cases and we moved to implicit Euler with matrix-free AD when residual convergence was not obtained for the case.

4.2 DLR TAU Code

Considered one of the predecessors of the new solver CODA, the legacy DLR TAU-Code is a finite-volume solver for the compressible flow equations on unstructured or hybrid grids [2].

Spatial discretization: Unlike CODA, TAU uses a cell-vertex approach by evaluating the flux balances on a dual-cell representation generated in a pre-processing step of the primary grid. Moreover, the mean flow is typically discretized using a central flux scheme with either scalar or matrix-valued artificial dissipation, while the turbulence equations employ the same scalar upwind flux as CODA. For 2^{nd} order, this flux takes linearly reconstructed face values based on Green–Gauss gradients, which are limited by a modified formulation of the Barth–Jespersen limiter [21].

Boundary conditions: Concerning the implementation of the boundary condition, a strong formulation of the boundary condition is the default, but a flux-based weak boundary condition was also studied as well as a hybrid wall function which is designed to be applicable also on meshes with $y^+ < 1$ and should then be in close agreement with the strong boundary condition (see [22]). In TAU, a half cell surrounding the wall node is used, i.e., the wall node is located at the wall, whereas the first node above the wall is associated with the center of the second dual grid cell.

Turbulence models: The SST model is available in both main versions (1994 and 2003) using the standard (non-logarithmic) form of the length-scale variable ω. However, for the present study an ad-hoc $ln(\omega)$ formulation was implemented for reference. As no limiter attenuation in smooth flow regions is applied, TAU's spatial turbulent scheme compares best to CODA, if the latter uses smallest possible K_{sd} values for the turbulence variables.

Time integration: Steady time integration relies on an explicit Runge-Kutta scheme or a semi-implicit Backward-Euler scheme described in [23], where the linear system is only approximately solved using a lower-upper symmetric Gauss–Seidel (LU-SGS) with simplified Jacobians, leading to a much weaker implicitness compared to CODA. A full approximation storage (FAS) multigrid method can be applied to improve convergence.

5. Simulation setup and cases

The section describes the cases covering different flow regimes such a subsonic, high-lift, transonic and information on the grid families used for the mesh convergence studies. Two cases are chosen from the NASA TMR [2] website, one research airfoil and one industrial airfoil are chosen to show the differences of the two formulations.

5.1 2D NACA4412 airfoil in subsonic highlift

One of the validation cases provided in the TMR website for "essentially incompressible" flows is the 2D NACA4412 airfoil [3] with a large sequence of nested grids from the same family. The geometry of the airfoil is defined analytically using the formulae published by Jacobs, Ward and Pinkerton (1933), by Abbott and von Doenhoff (1949), and others. The flow conditions for the case are: Reynolds number of $Re = 1.52 \times 10^6$, Mach number $M = 0.09$ and an angle of attack of $\alpha = 13.87°$ there appears a trailing edge separation. The reason for this was to use, for verification purpose, the reference data on the TMR website [4]. However, concerning validation and comparison with wind tunnel data, these conditions cannot be recommended, as described in [24].

We choose this airfoil due to the availability of a grid family and the subsonic nature of the case that could serve as a starting point for our comparison studies of the log form vs the non-log form. The grid family consists of 5 structured meshes with C-topology connecting to itself in a 1-to-1 fashion in the wake. The grid is stretched in the wall normal direction with 1025 points in the airfoil surface for the finest grid and 65 points for the coarsest grid. The grids range from 1793×513 as the finest grid to 113×33 as the coarsest grid with each coarse grid is exactly on every other point of the next finer grid as listed in the Table 2

Although the CODA simulations ran successfully for the settings of the validation case, the TAU simulations failed to converge with a steady-state RANS simulation and required an unsteady simulation procedure to converge to the steady-state solution. As our main purpose is not validation of the model or the code, we modified our settings to use a Mach number of $Ma = 0.25$ and $\alpha = 10°$ where the separation still happened at around 99% of the chord but not as strong as the validation case. The results described in section 6.2.1 use the modified flow conditions. In addition to grid convergence of boundary integral

[2] https://tmbwg.github.io/turbmodels/
[3] https://tmbwg.github.io/turbmodels/naca4412sep_val.html
[4] https://tmbwg.github.io/turbmodels/index.html

Grid level	No. of elements	No. of points on the airfoil	Approx. $y^+(1)$
L1	3729	51	1.0
L2	14,625	129	0.5
L3	57,921	257	0.2
L4	230,529	513	0.1
L5	919,809	1025	0.05

Table 2: Details for the subsonic NACA4412 airfoil grid family

quantities, we also investigated the surface integral quantities like coefficient of skin friction C_f and coefficient of pressure C_p. Due to the subsonic nature of the case, we encounter the pseudo-laminar region where the usage of the realizability limiter caused the difference between ω and $\ln(\omega)$ formulations.

5.2 2D Multi-Element Airfoil (2DMEA)

The 2D multi-element airfoil case as specified on the Turbulence Modeling Resource Website [5] [25] is a common verification case for turbulence model implementations in CFD codes. The geometry is a special 2D cut from the wing of the NASA Common Research Model in high-lift configuration (CRM-HL) with both the slat and the flap deployed. While the Reynolds and Mach number used in this study correspond to the specifications on [25], i.e. $Re = 5 \times 10^6$ and $M = 0.2$, the angle of attack is intentionally reduced from $\alpha = 16°$ to $12°$ in order to facilitate convergence to a steady state for different variants and settings of the SST model. Also at this angle of attack, the flow features a complex interaction of local separation in the coves of the slat and the wing, confluent shear/boundary layers on the main wing and the flap, as well as incipient pressure-induced separation on the flap. Since neither (experimental) validation data, nor published numerical reference data from the SST model exist for this test case, the present study purely focuses on sensitivities of the logarithmic length-scale formulation w.r.t. modelling details and numerical resolution.

To study the effect of grid resolution on the different variants of the SST model we consider the unstructured grid family II provided by NASA Ames [25], with overall and near-wall resolutions given in Tab. 3. [6]

Grid level	No. of elements	Approx. $y^+(1)$	Approx. stretching r
L1	138,833	2.0	1.25
L2	252,945	1.4	1.17
L3	388,323	1.0	1.12
L4	755,509	0.7	1.08
L5	1,375,004	0.5	1.06
L6	2,583,514	0.35	1.04
L7	4,839,196	0.25	1.03

Table 3: Resolution parameters of grid family II for the 2DMEA case (adopted from [25]).

The simulations that are presented in Sec. 6.2.2 employ CODA using the SST model with logarithmic and non-logarithmic (original) formulation of the length-scale equation. The investigation focuses on the behaviour of integral aerodynamic coefficients like lift and drag under grid refinement, but also studies the influence of the near-wall resolution, i.e. $y^+(1)$, on the skin friction.

[5] `https://tmbwg.github.io/turbmodels/index.html`

[6] Note that the element count that is relevant for CODA differs slightly from the number of points given on [25].

5.3 Transonic flow around research airfoil AC-05-12p6

In the transonic regime, we chose a 2D airfoil which was recently developed as a part of the DLR-internal project ACTIVATE. The geometry was designed to obtain a strong adverse pressure gradient on the upper side downstream of the shock when approaching the trailing edge. The boundary-layer flow experiences a pressure-induced separation at around $x/c \approx 0.88$. The flow conditions for this case involves Reynolds number of $Re = 3 \times 10^6$, Mach number $Ma = 0.733$ at an angle of attack $\alpha = 3°$. A family of three structured grids was generated for this case with each grid having an approximate $y^+ = 0.05$ and consisting of 139576, 372176 and 1542886 elements respectively. While investigating the surface integral quantities for the transonic cases, the dependence of the $\ln(\omega)$ variant with respect to the gradient limiter settings became very visible due to the movement of the shock location with respect to the grid refinement. The need for $\ln(\omega)$ to have a strong gradient limitation on the turbulent variables is still not yet completely understood.

5.4 Industrial transonic airfoil

An industrial transonic airfoil was chosen mainly to study the effects of the two formulations in industrial grade grids. The flow conditions used for setting up this case were $Re = 4.5 \times 10^6$, at transonic value of Ma lower than 0.75 (which cannot be specified here) at $\alpha = 3.1$. Despite the relatively low incidence angle, the boundary-layer flow on the upper and lower side is subjected to significant favourable and adverse streamwise pressure gradients in non-equilibrium conditions due to the surface geometry to obtain increased lift by rear loading. The pressure gradient in non-equilibrium causes a deviation of from the universal solution of a flat plate turbulent boundary layer in zero-pressure gradient, and a finer resolution of the near-wall region is expected.

In a precursor study, a detailed mesh convergence study was performed. Several hybrid grids were generated using the mesh generation tool Centaur involving systematic refinement in predefined boxes in the trailing edge region and in the wake, on the upper side inside and outside the boundary layer to resolve the shock, and in the leading edge region. The geometry was used from a wind-tunnel model whose blunt, sharp-edged trailing edge thickness was $z/c = 0.006$. It was found necessary to use at least 14 nodes on the blunt trailing edge for the cell-centered scheme of CODA and for the dual-grid approach if using the central scheme with scalar dissipation. Otherwise, a significant effect of shock movement compared the the grid-converged solution was found. In the present study, a sufficiently grid-converged resolution was used in the streamwise direction of the boundary layer as well as in the regions of leading edge, shock and wake. Then grids with a different resolution of the boundary layer were considered by (1) changing the number of layers while keeping $y^+ = 0.1$ of the first layer constant as well as the thickness of the hexahedral boundary layer mesh, and (2) changing the spacing y^+ of the first layer while keeping the boundary layer mesh thickness constant.

The aim was to study the near-wall region and the outer edge of the boundary layer to analyse the different resolution requirements in these regions required by the two formulations. As this was one of the cases with the industrial focus, any small deviation between the two codes CODA and TAU and between the two formulations ω and $\ln(\omega)$ needed to be explained due to the industrial certification requirements.

6. Results

6.1 Farfield decay

As described in Section 3.4, the k–ω SST turbulence model and similar RANS turbulence models are characterized by a decay in turbulence from the imposed freestream values to the levels generated in the vicinity of the body, where the imposed freestream condition should not influence the solution in the near-field region. However, the log formulation of this implementation shows a particular decay effect compared to TAU, as shown in Figure 1. The eddy viscosity ratio field is non-uniform presenting streak-like structures aligned with the streamwise direction. Additionally, the weak imposition of the boundary condition does not strictly enforce the prescribed freestream value of 0.1, but results in a value closer to 0.25. This level remains slightly elevated in the near-field region compared to expected results from TAU. Nevertheless, these differences have been shown not to influence the near-field solution, with pressure and skin-friction distributions remaining unaffected.

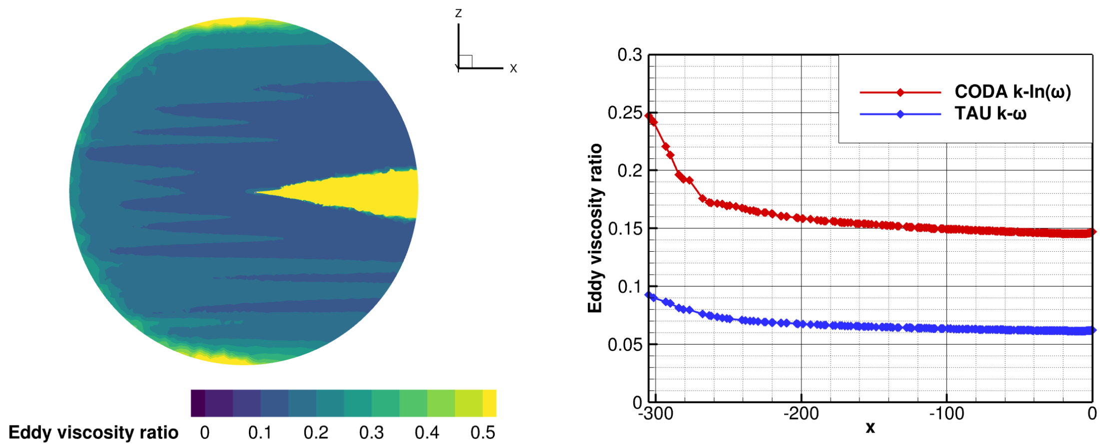

Figure 1: Eddy viscosity ratio obtained with the SST turbulence model for a high speed aircraft: contour field of log formulation in CODA (left) and streamwise variation along a line from freestream to the aircraft of log and non-log formulation, in CODA and TAU respectively (right).

During the first attempts to fix the robustness of the new solver, we identified the role of sustaining turbulence in stabilizing the solver. In this process the shielding function was developed to improve the results as most of our simulations did not converge without using sustaining turbulence. While trying to understand the influence of sustaining turbulence to increase solver robustness, we compared several simulation results when the sustaining turbulence is used and when it is not used. To our surprise, sustaining turbulence helped to increase the robustness of the $\ln(\omega)$ formulation but not the ω formulation. Decreasing the background turbulence while still using sustaining turbulence reduced the robustness of the solver. Investigating the converged solutions from various simulations, we observed the low levels of ω in the background field while using the $\ln(\omega)$ formulation which was not visible for ω formulation.

6.2 Global mesh convergence study

In the following subsections, the spatial resolution requirements are compared between the ω-based version and the $\ln(\omega)$-based variant. In industrial applications for the flow around a complex aircraft in 3D, mesh convergence studies can hardly be afforded, in particular not using a systematic global grid refinement study (see [26]). Instead best-practice guidelines for the automatic mesh generation are used. Such guidelines are for the spacing y^+, for the number of nodes in the boundary-layer mesh (consisting of hexahedral or prismatic elements) and the wall-normal stretching factor q, the number of nodes on sharp-edged blunt trailing edges, the stream-wise spacing Δx on wings, the resolution of the nose region of wings, in the region above and below the airfoil where shocks are expected, etc.

Here, on the one hand sequences of globally refined meshes are used to compare the grid convergence behaviour of the ω and the $\ln(\omega)$ variant. Moreover, a detail study of the resolution requirements for the boundary layer mesh is performed.

The mesh convergence studies for the cases - 2D NACA4412 airfoil (subsonic with minimal trailing edge separation), 2D Multi-element airfoil (subsonic high light conditions) and Activate airfoil 05-12p6 (transonic flow conditions with shock) are presented in this section. The first two cases use grids from NASA TMR as described before in section 5 where the meshes had been generated for a systematic global mesh convergence studies. For the transonic research airfoil, a family of grids was generated with a global refinement strategy for the purpose of this study to understand the influence of shock location under grid refinement.

6.2.1 2D NACA4412 airfoil

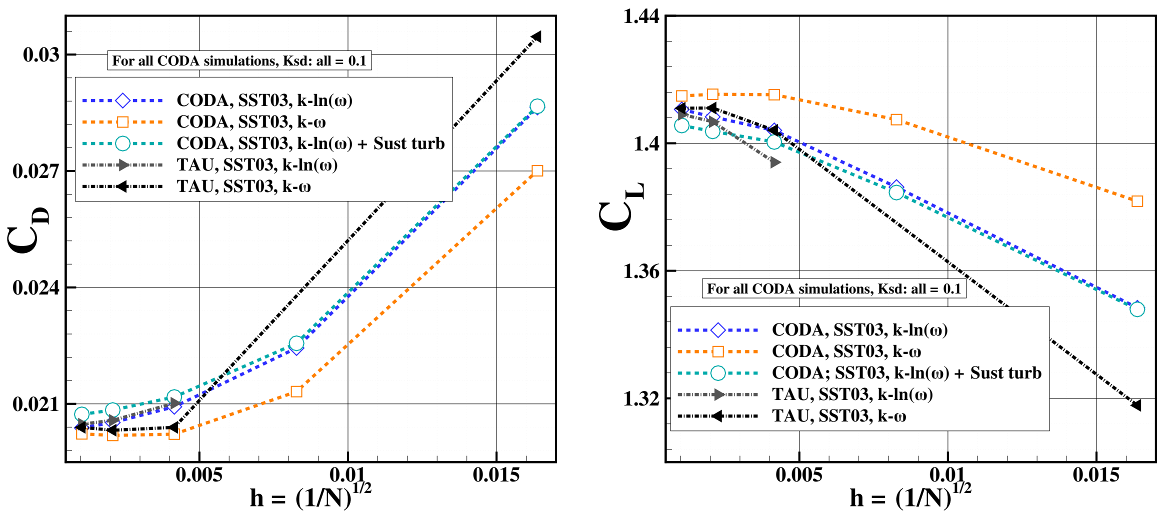

Figure 2: Mesh convergence for the 2D subsonic NACA4412 airfoil for SST2003$-\omega$ vs SST2003$ln(-\omega)$. Convergence of - left: coefficient of drag C_D, right: coefficient of lift C_L.

The 2D NACA4412 airfoil as described in section 5.1 was the first case we focused for the mesh convergence study using the grids provided in the table 2. The results of the mesh convergence studies performed on NACA4412 for the log ($\ln(\omega)$) vs the non-log (ω) form are shown in the figure 2. The case was also simulated with the legacy solver TAU and the coefficients of drag C_D and lift C_L are compared. Even on the finest grid, some differences are visible, and hence grid-convergence has not been achieved on the finest mesh. On the other hand, all results are converging towards each other. The simulations labelled "Sust turb" with the log form used the wake preserving sustaining turbulence as described in the section 3.4.1. We can observe from the plots in figure 2 that usage of sustaining turbulence did not vary the results in the coarser meshes and a slight deviation occurs in the finest meshes. Note that the coarse meshes are much coarser than used in industrial computations. On the coarsest two meshes, none of the length-scale versions and none of the solver is significantly better results. When we compare the results between the two solvers, the deviations of the log form appears to be consistent in the fine meshes. As some simulations did not converge, the deviations in the coarse meshes cannot be concluded well. If we compare the log form in CODA and non-log form in TAU, we would still see differences when the mesh is not fine enough.

6.2.2 2D Multi-Element Airfoil (2DMEA)

As outlined in Sec. 5.2, a grid sensitivity study was conducted for the subsonic flow about the 2D multi-element (high-lift) airfoil at $\alpha = 12°$, utilizing the unstructured/hybrid grid family II provided on the TMR website [25]. CODA results using the SST 2003 model both in standard and logarithmic formulations for the length-scale variable ω are considered.

The study focuses first on the development of the primary aerodynamic coefficients, i.e. lift C_L and drag C_D, under systematic grid refinement according to Tab. 3. The half-logarithmic plots in Fig. 3 reveal principal convergence to consistent results with increasing resolution, but also a remarkable wide spread between the logarithmic and the standard formulation.

While the $\ln(\omega)$-variant yields a monotonic lift and drag convergence with an overall even and mild

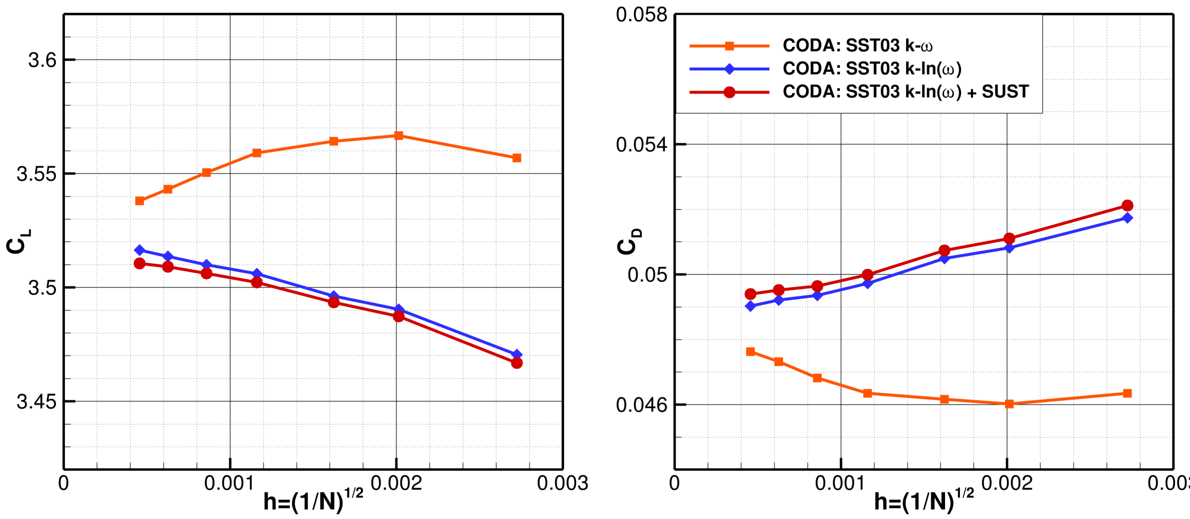

Figure 3: 2DMEA case: Mesh-resolution dependency of lift (left) and drag (right) coefficients for different SST 2003 variants in CODA.

(log-linear) gradient, the ω-based results change the convergence direction and show a larger sensitivity (gradient) than $\ln(\omega)$ on the finest grid levels. It should be noted that this mesh family is not adapted to the specific requirements of ω-based models, which would require values of $y^+(1)$ significantly less than 1 for a mesh-independent skin friction.

This is illustrated in Fig. 4, which shows the skin-friction coefficient c_f on the main-wing upper side close to the leading edge that are computed on different grid levels. While the $\ln(\omega)$ variant yields virtually grid-independent c_f already on grid level L3 ($y^+(1) = 1$), the ω formulation indicates ongoing changes even with the finest resolution L7 ($y^+(1) = 0.25$), in line which further studies in Sec. 6.3.1.

While the $y^+(1)$ sensitivity mainly contributes to C_D, the variation of C_L under mesh refinement is mostly affected by the outer boundary-layer development (i.e. thickness) and possibly separation. To study this, consider the pressure distributions for one exemplary coarse grid level, L3, in Fig. 4 (right). Despite high qualitative consistency between both SST variants, the $\ln(\omega)$-version shows a slightly delayed pressure recovery on the upper flap side (see the zoomed-in area) just upstream of a small separation (not shown here, but visible in c_f). This indicates a slightly stronger thickening of the trailing-edge boundary layer, which affects the global circulation sufficiently to yield a difference in lift of almost 2% on this grid level.

Although the complexity of the flow makes a further break-down into individual sensitivities difficult, it can be noted that, for the present test case on practical grids (i.e. $y^+(1)$ around 1), the $\ln(\omega)$ variant exhibits a more uniform and less pronounced grid sensitivity overall than the standard variant. Adding the sustaining turbulence terms of Sec. 3.4 to the $\ln(\omega)$ model ('+ SUST') only adds a small offset in Fig. 3 which, however, leads to slightly altered grid-converged lift and drag, if a rough (visual) linear extrapolation of the log-linear curves is taken as a basis.

6.2.3 Transonic research airfoil AC-05-12p6

While performing verification studies for transonic airfoils, the use of stronger gradient limitation (as detailed in the section 4.1.1) for the log form ($ln(\omega)$) shifted the shock location while the non-log form (ω) did not seem to be depend as much on the limitation. Hence, mesh convergence studies were performed for a research transonic airfoil as described in the section 5.3 with varying the K_{sd} values for turbulence equations. Initially, a common $K_{sd} = 0.1$ was used for both mean flow and turbulence, then $K_{sd} = 10^{-14}$ was imposed only on the turbulence keeping $K_{sd} = 0.1$ for the mean flow such that its second order accuracy is preserved well.

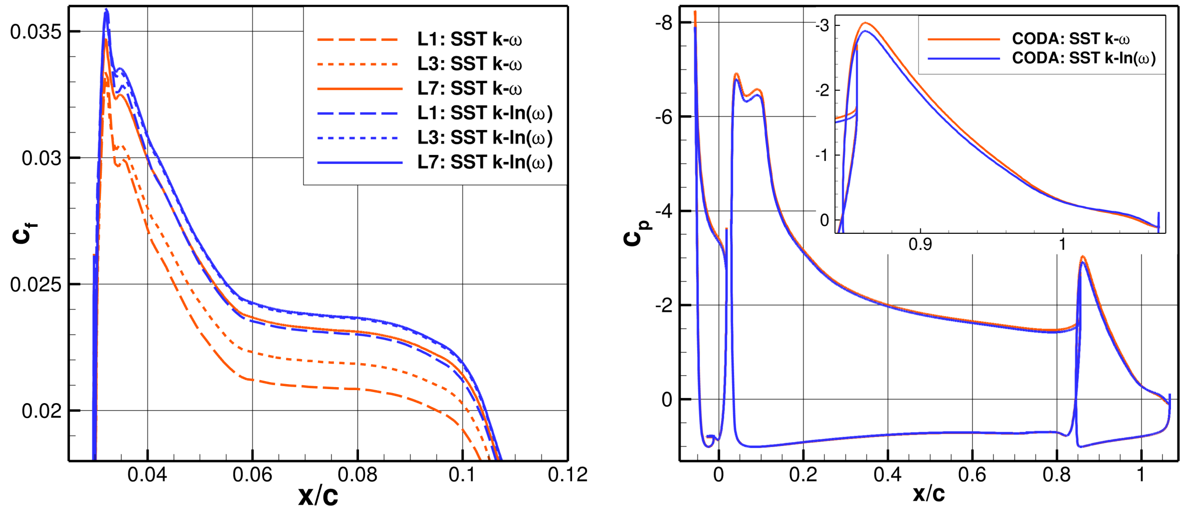

Figure 4: 2DMEA case: Mesh influence on skin friction near the leading edge of the main-wing upper side (left). Pressure distributions on L3 grid (right).

From the plots in the figure 5, one can observe that the integral values C_D and C_L which initially showed larger differences for the log form compared the non-log when using a common $K_{sd} = 0.1$ shifted when we impose a stricter limitation on the turbulence quantities. Once we use a $K_{sd} = 10^{-14}$ for the turbulence equations, the coarser meshes displayed results closer to the the fine grid results for the log form. The effect pronounced for both C_D compared to C_L where one can observe in the figure 5 that C_D even changes its convergence trend slightly and differs more compared to the non-log form. The results in the fine levels also differ when we change the limitation. However, the strongest difference appears in the coarse meshes. The non-log form did not seem to have such a drastic effect with increased limitation. It is important to note that the meshes used for this case are refined extremely (including in the far-field and trailing edge) that even coarse mesh is not in the range of the industrial grade meshes. Therefore the deviation of the integral coefficients in industrial grade meshes are expected to be much larger and comparing results between the two codes with two different formulations can be quite difficult for complex cases with industrial grade meshes.

When we further observe at the shock location using the surface integral quantities such as the coefficient of pressure C_p and the coefficient of skin friction C_f distributions as displayed in the figure 6, we see the shift in the shock front when we impose strict limitation ($K_{sd} = 10^{-14}$) for the turbulence equations in the log form. On the other hand, the non-log form shows very minimal dependency. This shift is observed not only in the shock location but also appears in the separation location of the flow as shown in the figure 7. This implies that the entire entire solution field behaves differently when a stronger limitation is not imposed for the log form. However, these differences were found to appear only for the transonic flows which we tested. The convergence studies for NACA4412 and 2D-MEA airfoils were repeated and the effect was not observed for the subsonic cases as seen in the figure 8.

The reason behind the dependency of the log form formulation is not yet known and it remains as one of the key details while using the log form so that the coarser meshes can provide us results with lesser error compared to the "almost mesh converged" solution. Further understanding of this behaviour of the log-form can be understood by looking closer the non-linear dynamics of a shock with respect to the gradients of the log form leading to addition or cancellation of some discretization errors. Due to time constraints, these studies are meant for the future work.

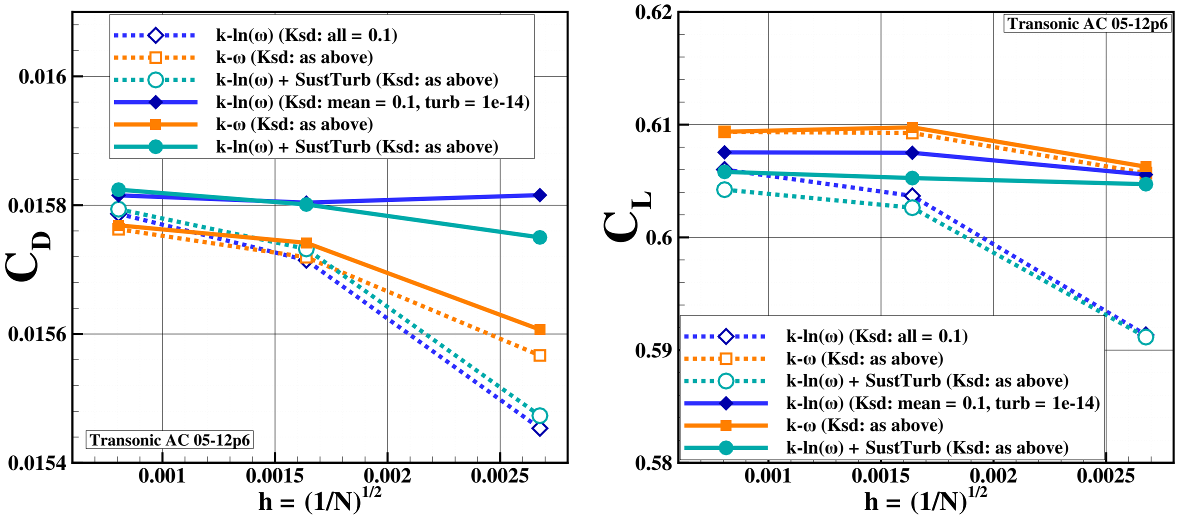

Figure 5: Transonic AC 05-12p6 airfoil: Mesh convergence of coefficient of drag (C_D) in the left and coefficient of lift (C_L) in the right of ω vs. $ln(\omega)$ when the gradient limitation (K_{sd} value) is varied for the turbulence equations.

6.3 Boundary layer resolution for transonic flow around an industrial supercritical airfoil

For the performance prediction of an aircraft, the prediction of viscous drag and hence of the C_f level are an important part. In order to study the grid-resolution requirements for a non-equilibrium flow in stream-wise changing pressure gradient at the verge of separation compared to the grid-requirements for a turbulent boundary layer flow over a flat plate at zero pressure gradient, an industrial relevant research airfoil is used. For this reason, absolute values cannot be shown, nor can be C_p or C_f distributions for the full airfoil. However, the effects of the length-scale formulation and the grid-requirements can be clearly demonstrated.

The y^+-values of the different meshes are given here for the dual-grid approach of TAU. The first computational node is in the center of the first off-wall control volume, below which there is a half cell with the corresponding wall point. In the cell-centered approach used in CODA, the computational node being the center of the first control volume (which is adjacent) to the wall is at half this y^+ value.

While performing our numerical studies, we also observed that there were still some unexplained differences in the results of the two formulations with respect to the shock location. We suspected them to arise from the mesh resolution in the near wall region, boundary layer and the boundary layer edge. To study these in detail, further mesh studies were performed involving only local refinements in the different regions of the boundary layer. An transonic industrial airfoil was used for these studies and we focus on the coefficient of skin friction C_f variations in our results.

6.3.1 Resolution of the near-wall region and y^+-requirements

First a mesh study with a variation of the y^+-values was performed. The results for C_f at a position in the fully developed turbulent boundary layer on the upper side of the airfoil, sufficiently upstream of the shock, are considered. Figure 9 (left) shows the results for TAU for the k-ω model. A trend of mesh convergence with respect to y^+ can be seen from the almost robust prediction for $y^+ \leq 0.1$. For $y^+ = 0.2$, some grid effect can be seen, which increases on the coarser meshes. For $y^+ = 1.6$, the level of C_f is almost 4 % too small. The predicted values for C_f are decreasing for increasing y^+ values. For the cell-centered method in CODA, figure 9 (right) shows a similar behaviour. On the meshes with y^+ of 0.8 and 1.6, the numerical error is found to be even a little larger than for the dual-grid approach, which

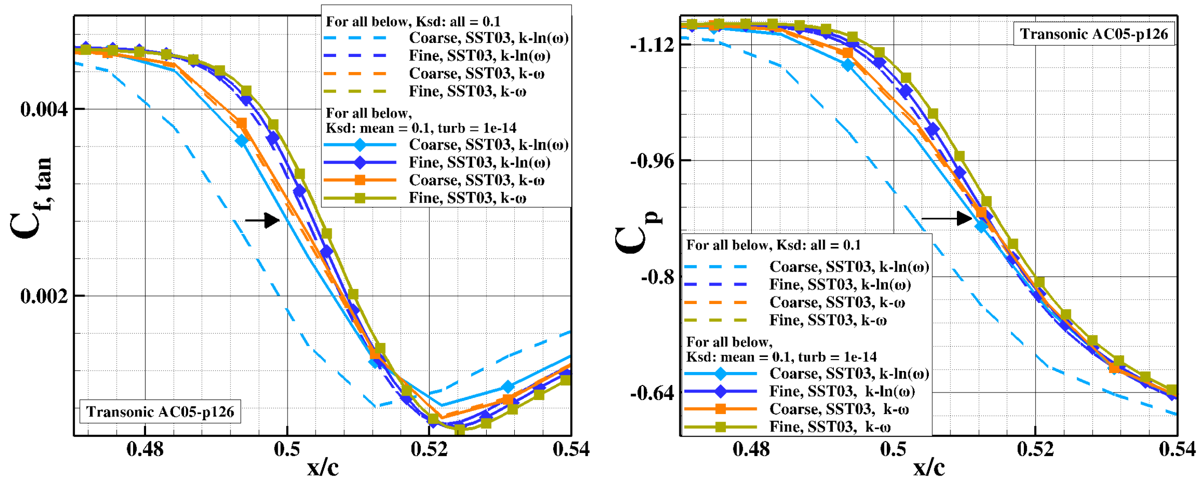

Figure 6: Transonic AC 04-12p6 airfoil: Shift of shock location when gradient limitation (K_{sd}) value is changed for the $ln(\omega)$ formulation compared to ω formulation in the coefficient of tangential skin friction $C_{f,tan}$ distribution (left) and the coefficient of pressure C_p distribution (right).

requires further investigation.

Then consider the results for the $\ln(\omega)$-based model. First, mesh sensitivity on the finest meshes $y^+ \leq 0.1$ is found to be smaller than for the ω-based model. The mesh sensitivity on the coarser meshes is remarkably small even for $y^+ = 1.6$. Another observation worth mentioning is that, for larger y^+-values, the C_f-values are increasing, whereas they were found to decrease for the ω-based model. This observation is important when assessing the difference between different CFD solver and different length-scale equation models on a mesh which is not mesh converged in terms of y^+, say, $y^+ = 0.8$. Then the deviation in C_f between ω and $\ln(\omega)$ appears to be twice the individual numerical error compared to the y^+-converged solution, as the numerical errors are additive due to their different signs.

The comparison between the different CFD solver and the different length scale equation are shown in figure 10 (right). When using the same flow solver CODA, then the deviation in C_f on fine mesh between ω (for $y^+ = 0.01$) and $\ln(\omega)$ is below 0.15 %. However, recall that the ω-based solution for CODA for this mesh is not yet mesh converged with respect to y^+. The dual-based approach TAU gives a slightly lower value of 0.44,% for C_f on the finest mesh.

6.3.2 Resolution of the boundary layer

The consider the variation of the number of cells in wall-normal direction while keeping $y^+ = 0.1$ constant. This was achieved by increasing the stretching factor q used in the wall-normal node distribution. The thickness of the boundary layer of hexahedral elements was kept constant at a value of around $0.062c$. Then the boundary layer was found to be fully located inside the boundary layer mesh, even near the trailing edge downstream of the shock.

The results for the ω-based model using CODA are shown in figure 11 (left). For the meshes with equal or less than 70 nodes in wall-normal direction, a numerical error in C_f is found. The C_f values are found to be lower than for the fine meshes, and the deviation can be up to 3 % on the mesh with 42 nodes in wall-normal direction. Next consider the results for the $\ln(\omega)$-based model for CODA. The observation is similar, although the numerical error is found to be slightly smaller than for the ω-based model on the coarse boundary layer meshes. This result is seen to be important. In [27] the concern was raised as to whether the variable transformation to $\ln(\omega)$ could lead to an additional numerical discretisation error near the boundary layer edge or outside the boundary layer due to the gradient term

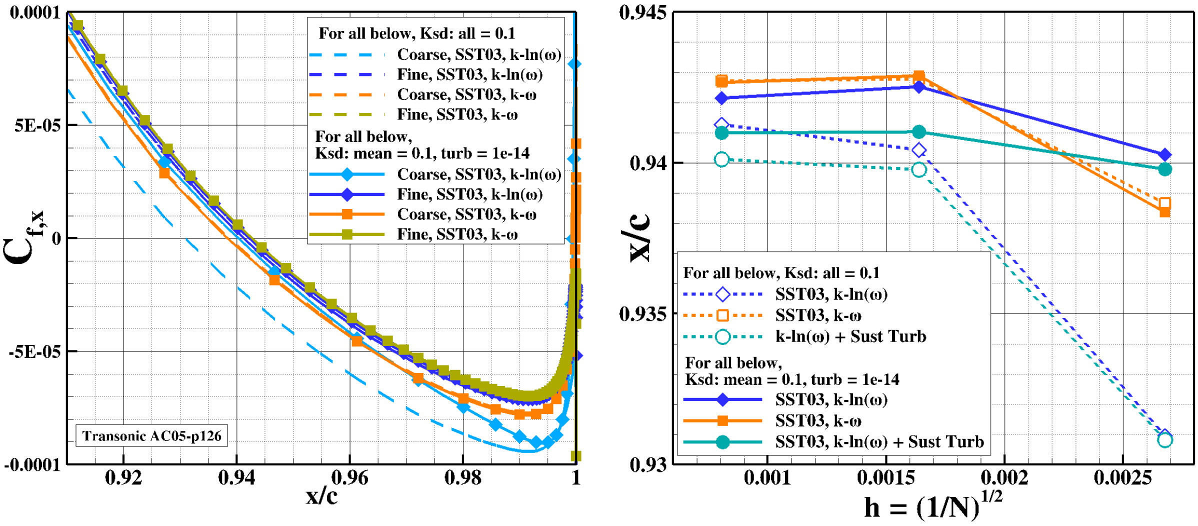

Figure 7: Transonic AC 04-12p6 airfoil: Shift of separation location when gradient limitation (K_{sd}) value is changed for the $ln(\omega)$ formulation compared to ω formulation in the coefficient of skin friction $C_{f,x}$ distribution (left) and grid convergence of the location x/c (right).

involving $\partial\hat{\omega}/\partial x_j \partial\hat{\omega}/\partial x_j$ as given in the Eq. (14). The present result does not give support or indication concerning such concern.

Then consider the results for the $\ln(\omega)$-based model with sustaining turbulence in figure 12 (left) for CODA. A low free-streamvalue of $\mu_t/\mu = 0.1$ was used. The results are similar in trend to the $\ln(\omega)$-based model, but the magnitude of the numerical error is even smaller than for CODA for the ω-based model on the coarser meshes. Moreover, this figure shows that the result for C_f for the $\ln(\omega)$-based model with such low free-stream value for μ_t/μ deviates by only 0.06 % from the solution without sustaining turbulence.

7. Conclusions

The effect of using a logarithmic formulation for the length-scale equation for the SST two-equation RANS model was presented. The transport equation of the log form ($\ln(\omega)$) follows by a transformation of the original equation for the specific rate of turbulent dissipation ω. Both formulations are equivalent on the level of a continuous partial different equation, but behave differently on a discrete level, i.e., when used in a numerical flow solver based on the finite-volume method. The question is as to whether the log-formulation has advantages in terms of grid-resolution requirements and/or robustness.

The effect of the length-scale variable version on robustness was found to be connected to other details used in the implementation. The standard non-log (ω-based) formulation showed a more gentle decay behaviour at the far-field boundary. The log-omega form lead to lower far-field values and steeper gradients near the interface between turbulent boundary layer and wake flow and the inviscid free stream. The option of using sustaining turbulence was found to be a helpful method to enhance robustness. When using the wake preserving sustaining turbulence, then the effect on the solution accuracy, i.e., the deviation between with and without sustaining turbulence, for clean wing configurations is found to be clearly smaller than other sensitivities.

Under mesh refinement, the solution for the log form ($\ln(\omega)$) and the solution for the non-log (ω) were confirmed to converge to similar solutions for all the two-dimensional cases presented in this work irrespective of the type of meshes (structured or unstructured) and their refinement (global or local). However, even on the finest mesh level still small differences in the surface solution for the pressure and for the skin-friction coefficient as well as for the integral force coefficients of lift and moment can be seen.

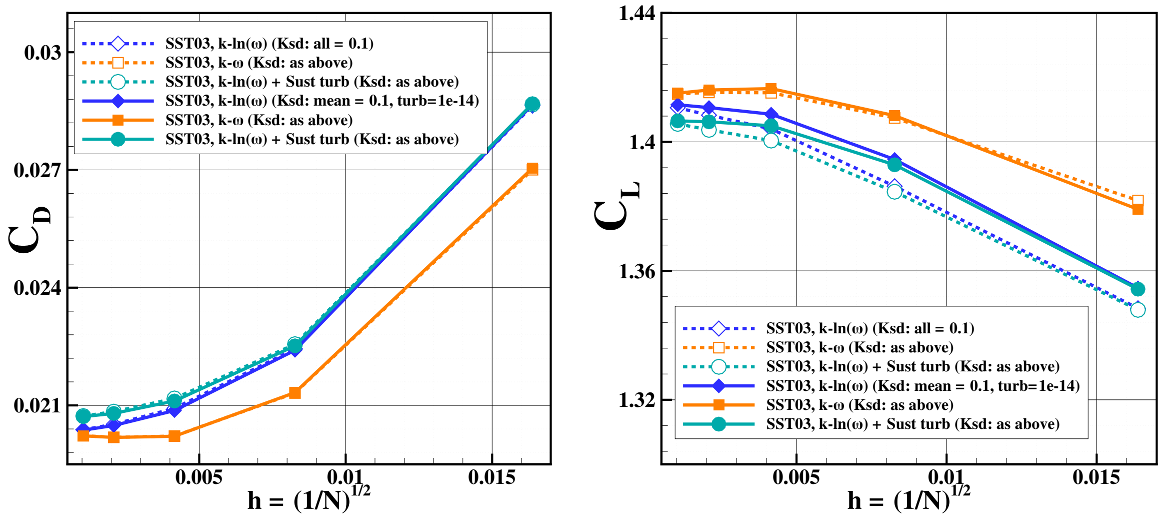

Figure 8: NACA4412 airfoil: Grid convergence of C_D and C_L when the gradient limitation (K_{sd}) value is changed for the $ln(\omega)$ formulation compared to ω formulation.

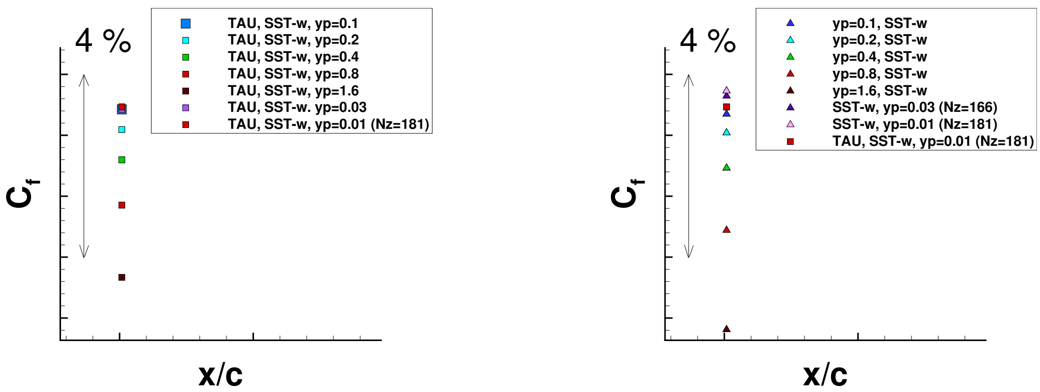

Figure 9: Transonic airfoil flow. Sensitivity of C_f on the upper side upstream of the shock on $y^+(1)$ for SST k–ω with TAU (left) and CODA (right).

This is relevant for practical applications, as the spatial resolution on the finest 2D meshes was much finer than the resolution typically affordable in complex 3D aircraft configurations for industrial applications.

Concerning lift and drag coefficients, the deviation between the ω- and the $\ln(\omega)$-based solution on a coarse mesh was generally found to be almost twice as large as the deviation from the grid converged solution, as the sign of the numerical error can be opposite. Moreover, regarding the speed of grid convergence of the lift- and drag-coefficient towards the grid-converged value, none of the two length-scale forms were found to be clearly better.

Regarding the prediction of the surface distribution of the skin-friction coefficient, the log-variant enables to obtain almost the same accuracy on meshes with larger y^+-values of the first grid point. Moreover, the numerical error has opposite sign when comparing C_f between non-log (ω)- and log ($\ln(\omega)$)-version, as the former predicts significantly lower values for C_f, whereas the latter gives slightly higher values. Therefore, on a given grid with a non-small y^+-distribution, the deviation between $\ln(\omega)$ and ω appears to be much larger than the numerical error of the $\ln(\omega)$-version from the grid-converged result. Another observation is that a very similar constraints regarding the number of mesh points in wall normal direction were found for the ω and the $\ln(\omega)$ version. At least 70 layers should be used to resolve the boundary layer in wall-normal direction for both length-scale variable versions to obtain virtually grid-independent solutions.

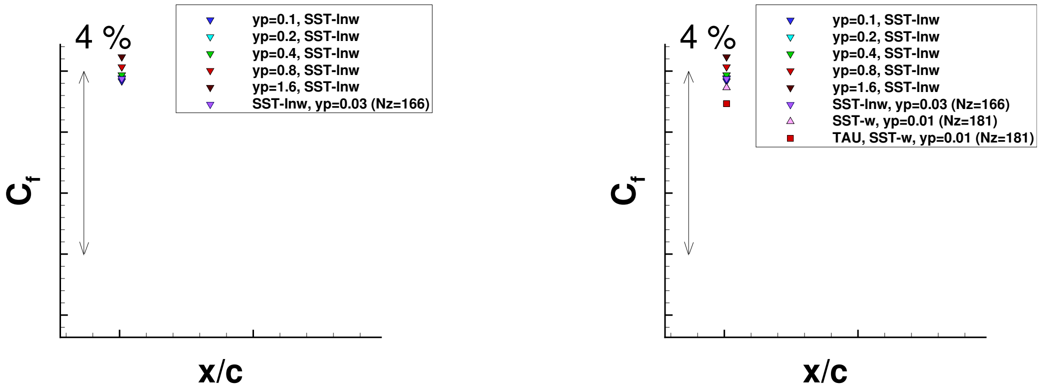

Figure 10: Transonic airfoil flow. Sensitivity of C_f on the upper side upstream of the shock on $y^+(1)$ for SST k–ln(ω) with CODA (left) and comparison with SST k–ω results (right).

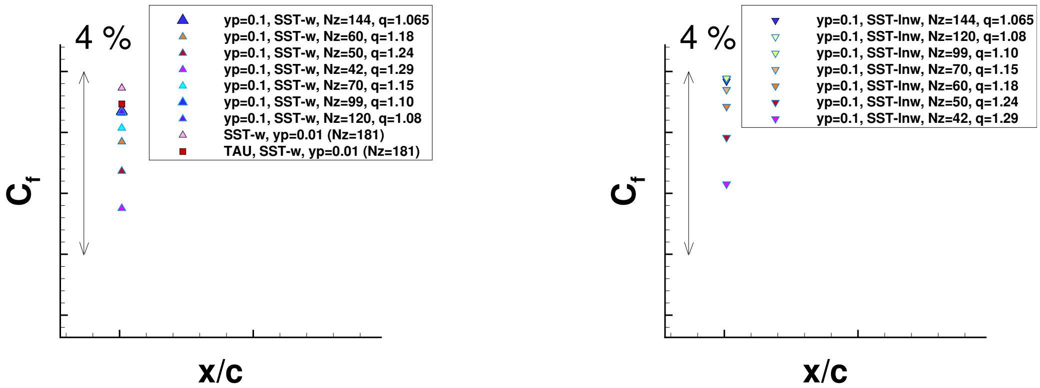

Figure 11: Transonic airfoil flow. Sensitivity of C_f on the upper side upstream of the shock on number of layers in the boundary layer mesh and the stretching-factor for the wall-normal point distribution for SST k–ω (left) and k–ln(ω) (right), both using CODA.

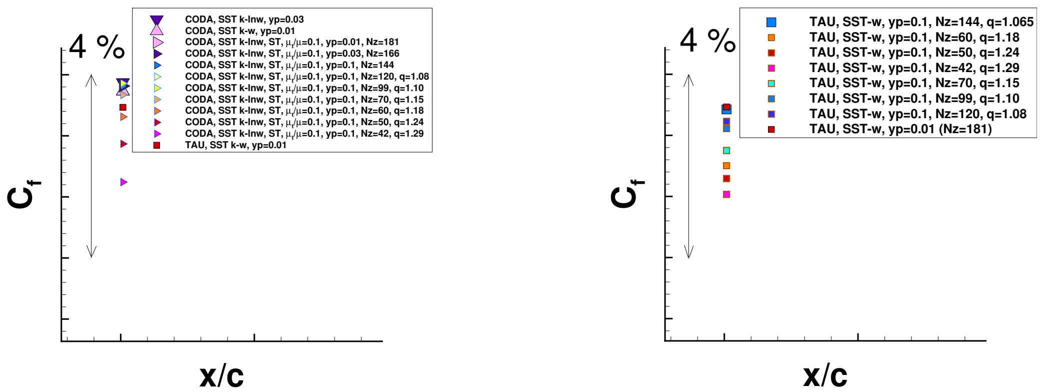

Figure 12: Transonic airfoil flow. Sensitivity of C_f on the upper side upstream of the shock on number of layers in the boundary layer mesh and the stretching-factor for the wall-normal point distribution. Left: Influence of sustaining turbulence. Right: Comparison between two solver CODA and TAU.

When comparing the sensitivity on the length-scale variable and the sensitivity of the overall numerical method by changing the flow solver, the numerical sensitivity of the log form of the equation is found to be larger and quite dependent on the solver settings such as the gradient limiters (K_{sd} values) and the implementation details of other limiters in the turbulence models such as the realizability constraints. The dependency on the gradient limiters of the log form also appears to be case-dependent and appears mainly when the flow regime is transonic and contains shocks. A stronger limitation of the log form was essential not only for increasing robustness but also the accuracy which is counter-intuitive. Further investigation is needed to understand this behavior of the log formulation which is aimed for future work. The log form of the equation is also used for other complex models like the Reynolds stress models (RSM) in the context of the SSG\LRR-RSM model. The future work also aims to study the influence of the gradient limiters across various turbulence models in the log form as a stricter limitation would be necessary for ensuring the convergence of the model.

Acknowledgements

The validation and robustness improvement campaign was performed under the collaboration of Airbus, DLR and ONERA under the name of task forces. We would like to acknowledge all the people (in addition to the authors) who contributed to several developments and testing during the task force organised for the two-equation turbulence models: Aimad Er-Raiy (Airbus Operations SAS, Toulouse), Bartolomeo Fanizza (ONERA), Johannes Löwe (AS-CAS-GÖ, DLR), Jens Jägersküpper (AS-CAS-BS, DLR), Markus Fertig (AS-RFZ-BS, DLR), Michael Saur (AS-TFZ-BS, DLR), Ralf Hartmann (AS-CAS-BS, DLR), Romain Olivanti (Airbus Operations SAS, Toulouse), Romain Laraufie (Airbus Operations SAS, Toulouse), Stefan Fechter (AS-RFZ-GÖ, DLR), Vamshi Togiti (AS-CAS-BS, DLR). The authors also gratefully acknowledge the scientific support and HPC resources provided by the German Aerospace Center (DLR). The HPC system CARO is partially funded by "Ministry of Science and Culture of Lower Saxony" and "Federal Ministry for Economic Affairs and Climate Action".

A. Realizability constraints in TAU

The realizability constraints used in CODA and TAU are derived based on the work by Durbin [15]. Let us consider the Reynolds stress tensor τ_{ij}^{turb} re-written as:

$$\tau_{ij}^{\text{turb}} = 2\overline{\rho}k\left(\frac{\widetilde{S}_{ij}}{\omega} - \frac{\delta_{ij}}{3}\right) \tag{21}$$

where $\widetilde{S}_{ij}$ denotes the traceless strain-rate tensor. For $\overline{\rho}k = 0$, τ_{ij}^{turb} trivially satisfies the realizability condition with zero eigenvalues. For $\overline{\rho}k > 0$, the eigenvalues of τ_{ij}^{turb} can become negative when ω becomes too small. Realizability can be restored by using a higher value of ω in the denominator of μ_t. Due to the positivity of $\overline{\rho}k$, it is sufficient to focus on the eigenvalues of the term inside the brackets.

Let us denote the eigenvalues of $\widetilde{S}$ as λ_1, λ_2 and λ_3. Since $\widetilde{S}$ is symmetric and traceless, its eigenvalues obey the following conditions:

$$\lambda_1 + \lambda_2 + \lambda_3 = 0 \tag{22}$$

$$\lambda_1^2 + \lambda_2^2 + \lambda_3^2 = \widetilde{S}_{ij}\widetilde{S}_{ji} = |\widetilde{S}|^2 \tag{23}$$

As these conditions are invariant under coordinate rotations, without loss of generality, let us assume that we are in the principal axes of $\widetilde{S}$ where it can be written as a diagonal matrix with its eigenvalues along the diagonal. The realizability condition then simplifies to:

$$\frac{1}{\omega}\max_i(\lambda_i) - \frac{1}{3} \leq 0 \qquad \Rightarrow \qquad \omega \geq 3\max_i(\lambda_i) \tag{24}$$

and all that is required now is an upper bound for $\max_i(\lambda_i)$.

Without loss of generality, suppose that $\max_i(\lambda_i) = \lambda_1$. It follows from Eq. (22) that $\lambda_1 = -(\lambda_2 + \lambda_3)$. Substituting this into Eq. (23) yields:

$$(\lambda_2 + \lambda_3)^2 + \lambda_2^2 + \lambda_3^2 = |\widetilde{S}|^2 \tag{25}$$

Let us define two constants a and b such that the following conditions hold.

$$\lambda_2 = \frac{a}{\sqrt{6}} + \frac{b}{\sqrt{2}}, \qquad \lambda_3 = \frac{a}{\sqrt{6}} - \frac{b}{\sqrt{2}} \tag{26}$$

Note that it is always possible to find such constants for any λ_2 and λ_3. Substituting these for λ_2 and λ_3 in Eq. (25) and simplifying leads to:

$$a^2 + b^2 = |\widetilde{S}|^2 \tag{27}$$

From $\lambda_1 = -(\lambda_2 + \lambda_3)$, we have:

$$\lambda_1 = -\frac{2a}{\sqrt{6}} \tag{28}$$

Since we seek the maximum value for λ_1, we must determine the minimum value of a. As Eq. (27) is simply the equation for a circle with radius $|\widetilde{S}|$ [7] , the minimum value of a is simply $-|\widetilde{S}|$ which in turn leads to:

$$\lambda_1 = \frac{2|\widetilde{S}|}{\sqrt{6}} \tag{29}$$

Substituting this result into Eq. (24) finally yields the lower bound for ω:

$$\omega \geq \sqrt{6}|\widetilde{S}| \tag{30}$$

This constraint can be applied by clipping ω directly in addition to the clipping described in section 3.1. Such a methodology was followed in the legacy solver DLR-TAU where the non-log form of the length-scale equation was used and is known as the Schwarz limiter in the solver.

B. Realizability constraints in CODA

In CODA, as we mainly use the log form of the equation, it led to differences in C_f distribution in the leading edge of subsonic cases compared to the non-log formulation as well as weird contours in some regions for the blending functions as described in section 3.2. An alternative was derived where we use the realizability constraint only in the eddy-viscosity ν_t.

If the eigenvalues of the Reynolds stress tensor, τ_{ij}^{turb}, are denoted by $\lambda_\tau^{(l)}$, they should satisfy the inequality $0 \leq \lambda_\tau^{(l)} \leq 2k$. Now, if we write the Reynolds stresses as:

$$\tau_{ij}^{turb} = 2\mu_t \left(S_{ij} - \frac{1}{3}\frac{\partial U_k}{\partial x_k}\delta_{ij} \right) - \frac{2}{3}\overline{\rho} k \delta_{ij} \tag{31}$$

then we get the constraint, $2\nu_t\lambda_{\max}^S \leq \frac{2}{3}k$ from Durbin's work [15]. Note that this constraint implies that the upper bound $0 \leq \lambda_\tau^{(l)} \leq 2k$ is automatically satisfied. Here $\lambda_{\max}^S$ is the maximum eigenvalue of the rate of strain tensor. The rate of strain tensor S_{ij} is symmetric and becomes purely diagonal in principal-axes coordinates. The diagonal elements, λ_α, $\alpha = 1, 2, 3$, are its eigenvalues and still satisfy Eq. 23 and Eq. 22 is satisfied when the flow is incompressible.

[7] Geometrically speaking, Eq. (22) represents a plane and Eq. (23) represents a sphere of radius $|\widetilde{S}|$. Their intersection produces the circle of radius $|\widetilde{S}|$ whose equation is given by Eq. (27).

In two dimensions (i.e., where $\lambda_3 = 0$, and therefore $\lambda_2 = -\lambda_1$)

$$2\lambda_\alpha^2 = |S|^2 \quad \Leftrightarrow \quad |\lambda_\alpha| = \sqrt{|S|^2/2} \tag{32}$$

and in three dimensions

$$|\lambda_\alpha| = \sqrt{2|S|^2/3} \tag{33}$$

Note that a factor of $\sqrt{2}$ is missing in Durbin's definition of $|S|$ compared to the implementation in CODA. Durbin's work also gives us two constraints $\overline{u_i'u_i'} \leq 0$ and $2k \leq \overline{u_i'u_i'}$ for all i. Moreover he specifies that the former is more stringent and that it requires $2\nu_t \max_\alpha \lambda_\alpha \leq \frac{2}{3}k$ while the latter relation requires $2\nu_t \max_\alpha \lambda_\alpha \geq -\frac{4}{3}k$. Hence, he continues his work with the former relation.

Also, it can be shown from his work that $\lambda_{\max}^S < \sqrt{2|S|^2/3}$. Therefore, if $\nu_{t,\text{limit}}$ is defined so that it satisfies the first inequality, then it will automatically satisfy the second of the following

$$2\nu_{t,\text{limit}}\sqrt{2|S|^2/3} < \frac{2}{3}k \quad \Rightarrow \quad 2\nu_{t,\text{limit}}\lambda_{\max}^S < \frac{2}{3}k \tag{34}$$

This gives the following conservative, sufficient condition for $\nu_{t,\text{limit}}$

$$2\nu_{t,\text{limit}}\sqrt{2|S|^2/3} \leq \frac{2}{3}k \Leftrightarrow \quad \nu_t \leq \frac{1}{3}\frac{k}{\sqrt{2/3}|S|} \leq \frac{k}{\sqrt{6}|S|} \tag{35}$$

The realizability limitation in CODA applied to μ_t of the SST2003 model as provided in the table 1 yields

$$\nu_t = \min\left(\frac{k}{\omega^*}, \frac{k}{\sqrt{6}\,S}\right) = \frac{k}{\max[\max(\omega, SF_2/a_1)\,,\,\sqrt{6}\,S]} \tag{36}$$

Note that in the above equation, S is not specified rather the work by Durbin is merely summarized. A factor $1/2$ due to lack of precise definition of S might arise. For this see the Schwarz limiter for ω in TAU in Eq. (30)).

Note that $1/a_1 = 1/0.3 = 3.333$ and $\sqrt{6} = 2.450$. Hence in a region where $F_2 = 1$ (which is inside the boundary layer), the limiter is not active. Hence it is expected that this modification does not affect the solution in the boundary layer. Outside the boundary layer where $F_2 < 1$, this limiter is expected to change the flow solution. Hence, we use the corrected version in CODA compared to the Durbin limiter in TAU.

References

[1] F. R. Menter. Two-equation eddy-viscosity turbulence models for engineering applications. *AIAA Journal*, 32(8):1598–1605, August 1994. Publisher: American Institute of Aeronautics and Astronautics.

[2] Dieter Schwamborn, Thomas Gerhold, and Ralf Heinrich. THE DLR TAU-CODE: RECENT APPLICATIONS IN RESEARCH AND INDUSTRY. In *ECCOMAS CFD 2006 CONFERENCE*, 2006. auf CD.

[3] Stefan Görtz, Tobias Leicht, Vincent Couaillier, Michael Méheut, Pascal Larrieu, and Steeve Champagneux. CODA: A European Perspective for a Next-Generation CFD, Analysis and Design Platform. In *NATO AVT-366 Workshop on Use of Computational Fluid Dynamics for Design and Analysis: Bridging the Gap Between Industry and Developers*, Mai 2022.

[4] F. Ilinca, J. F. Hétu, and D. Pelletier. A unified finite element algorithm for two-equation models of turbulence. *Computers & Fluids*, 27(3):291–310, March 1998.

[5] Sebastian Braun and Vamshi Togiti. *Robustness Improvements for a Differential Reynolds Stress*

Modeling Using a Logarithmic Formulation, pages 41–53. Springer International Publishing, Cham, 2025.

[6] Michael Müller, Hans-Peter Kersken, and Christian Frey. A Log-w Turbulence Model Formulation for Flutter Analysis with Harmonic Balance. In *16th International Symposium on Unsteady Aerodynamics, Aeroacoustics & Aeroelasticity of Turbomachines (ISUAAAT16)*, Toledo, Spanien, September 2022.

[7] Michael Müller and Christian Morsbach. A logarithmic w-equation formulation for tubulence models in harmonic balance solvers. In *ECCOMAS - - ECFD 2018 - 6th European Conference on Computational Mechanics (Solids, Structures and Coupled Problems) / 7th European Conference on Computational Fluid Dynamics*, Glasgow, UK, 2018.

[8] David C. Wilcox. Formulation of the k-w turbulence model revisited. *AIAA Journal*, 46(11):2823–2838, 2008.

[9] Florian R. Menter. Review of the shear-stress transport turbulence model experience from an industrial perspective. *International Journal of Computational Fluid Dynamics*, 23(4):305–316, 2009.

[10] F. Menter. *Zonal Two Equation k-w Turbulence Models For Aerodynamic Flows*.

[11] P. A. Durbin and B. A. Petterson Reif. *Statistical theory and modelling for turbulent flows*. John Wiley & Sons, Chichester, 2001.

[12] A. Hellsten. Extension of the k-ω-sst turbulence model for flows over rough surfaces. *AIAA Paper 1997-3577*, 1997.

[13] H. Grotjans and F. Menter. Wall functions for general application cfd codes. In *ECCOMAS 1998*, volume 1, pages 1112–1117, 1998.

[14] J. C. André, G. De Moor, P. Lacarrère, and R. Du Vachat. Turbulence Approximation for Inhomogeneous Flows: Part I. The Clipping Approximation. *Journal of the Atmospheric Sciences*, 33(3):476–481, March 1976. Publisher: American Meteorological Society Section: Journal of the Atmospheric Sciences.

[15] P.A. Durbin. On the k-3 stagnation point anomaly. *International Journal of Heat and Fluid Flow*, 17(1):89–90, 1996.

[16] Steve Evans and Sylvain Lardeau. *Validation of a turbulence methodology using the SST k-ω model for adjoint calculation*.

[17] Philippe R. Spalart and Christopher L. Rumsey. Effective inflow conditions for turbulence models in aerodynamic calculations. *AIAA Journal*, 45(10):2544–2553, 2007.

[18] Tobias Leicht, Daniel Vollmer, Jens Jägersküpper, Axel Schwöppe, Ralf Hartmann, Jens Fiedler, and Tobias Schlauch. DLR-Project Digital-X: Next generation CFD solver 'Flucs'. January 2016.

[19] Axel Schwöppe and Boris Diskin. *Accuracy of the Cell-Centered Grid Metric in the DLR TAU-Code*, pages 429–437. Springer Berlin Heidelberg, Berlin, Heidelberg, 2013.

[20] C.-C. Rossow. Enhanced runge-kutta/implicit methods for solving the navier-stokes equations. In Cameron Tropea, Suad Jakirlic, Hans-Joachim Heinemann, Rolf Henke, and Heinz Hönlinger, editors, *New Results in Numerical and Experimental Fluid Mechanics VI*, pages 202–209, Berlin, Heidelberg, 2008. Springer Berlin Heidelberg.

[21] Timothy J. Barth and Dennis C. Jespersen. The design and application of upwind schemes on unstructured meshes. In *AIAA 28th Aerospace Sciences Meeting*, volume 90, pages 1–12, 1990. AIAA Paper 90-0484.

[22] T. Knopp, Th. Alrutz, and D. Schwamborn. A grid and flow adaptive wall-function method for RANS turbulence modelling. *Journal of Computational Physics*, 220:19–40, 2006.

[23] R. P. Dwight. *Efficiency Improvements of RANS-Based Analysis and Optimization using Implicit and Adjoint Methods on Unstructured Grids. Dissertation*. PhD thesis, School of Mathematics, University of Manchester, 2006. [Also: DLR Forschungsbericht, ISSN 1434-8454, Report 2006-11], 2006.

[24] T. Knopp. Modification of the SSG/LRR-Omega Model for Turbulent Boundary Layers in an Adverse Pressure Gradients. *Flow, Turbulence and Combustion*, 111:409–438, 2022.

[25] Turbulence modeling resource for the validation and verification of turbulence models. `https://tmbwg.github.io/turbmodels/`, 2026. Accessed: 2026-05-05.

[26] T. Knopp, L. Eca, S. L. Toxopeus, D. Fritsch, A. Gargiulo, K. T. Lowe, C. J. Roy, G. Deng, M. Visonneau, and E. Guilmineau. Errors and uncertainties in cfd validation for non-equilibrium turbulent boundary layer flows at high reynolds numbers. *Journal of Turbulence*, 25, 2024.

[27] Stefan Langer and R. C. Swanson. On Boundary-Value Problems for RANS Equations and Two-Equation Turbulence Models. *Journal of Scientific Computing*, 85(1):20, October 2020.